Three-dimensional Simulations of Water-Mercury Anticonvection

Thomas Boeck[1], Alexander Nepomnyashchy[2,3] and Ilya Simanovskii[2]

Abstract: Anticonvection in a two-layer system of mercury and water is studied using three-dimensional direct numerical simulations with a Fourier-Chebyshev spectral method. The two fluid layers have equal thicknesses and are uniformly heated from above. Interface deformations and surface tension gradients are neglected. The quiescent state is replaced by steady hexagons upon increasing the heating from above. We investigate the destabilization of this primary convective pattern in a small and in a large computational domain upon increasing the temperature difference across the two fluid layers. For the large domain the convection cells become disordered at about twice the critical temperature difference for the onset of convection. The mean interfacial temperature spectrum shows a power-law behavior with an exponent somewhat larger than -4. Convection cells grow in size with increasing temperature difference.

Keyword: buoyancy convection, two-layer system

1 Introduction

Two-layer systems of immiscible fluids can display a variety of instabilities in the presence of temperature gradients. Local perturbations of the equilibrium state can be amplified when the flow induced by either buoyancy or Marangoni forces can overcome the damping effect of thermal and viscous diffusion. The classical cases are Rayleigh- and Marangoni instabilities when

the layers are heated uniformly from below, which have been at the origin of much research on nonlinear dynamics and pattern formation [Nepomnyashchy, Simanovskii, and Legros (2006)]. In the typical liquid-gas system, the flow in the gas is unessential for the instability mechanism. It is therefore frequently neglected. Heat conduction in the gas layer can then be approximately described through an effective thermal boundary condition at the interface with a suitably defined Biot number [Nepomnyashchy, Simanovskii, and Legros (2006)].

Remarkably, certain two-liquid systems can become unstable also by heating from above. Welander first noted that buoyancy forces can generate the so-called anticonvection when the thermophysical properties of the liquids are very different [Welander (1964)]. In contrast to the classical instabilites, the flow in both layers, and the mechanical coupling by the stress balance at the interface are essential for the instability mechanism. A suitable configuration for anticonvection requires a lower, dense liquid of high thermal conductivity combined with an upper liquid with considerably smaller heat conductivity. The instability mechanism can then be described by considering a rising fluid element in the lower layer approaching the interface. Because of continuity and mechanical coupling at the interface, a corresponding downward motion is generated in the upper liquid. This downward motion in the top layer carries warmer fluid towards the interface, whereby the temperature rises in the lower layer near the interface thanks to the high thermal conductivity of the lower liquid. This way, the rising fluid element in the lower layer can obtain an excess temperature relative to the mean (positive) temperature gradient and thereby sustain its motion through positive buoyancy. In the top layer, the downward flow is opposed to the buoyancy

[1] Fachgebiet Thermo- und Magnetofluiddynamik, TU Ilmenau, P.O. Box 100565, 98684 Ilmenau, Germany.

[2] Department of Mathematics, Technion – Israel Institute of Technology, 32000 Haifa, Israel

[3] Minerva Center for Nonlinear Physics of Complex Systems, Technion - Israel Institute of Technology, 32000 Haifa, Israel.

forces.

Welander analyzed the instability mechanism by means of linear stability theory. In his paper he identifies the pairing of water and mercury at temperatures below $18°$ C as a suitable system for anticonvection [Welander (1964)].

To the present date, no successful anticonvection experiments have been reported to the knowledge of the authors. Nepomnyashchy et al. recently studied the effect of heat sources or sinks on the interface between liquid layers [Nepomnyashchy, Simanovskii, and Braverman (2000), Nepomnyashchy and Simanovskii (2001), Nepomnyashchy and Simanovskii (2002)]. In this case, anticonvection can appear more easily, and the thermophysical properties of the liquids need not be as dramatically different as in the mercury-water case. Heat sources or sinks can, in principle, be produced by interfacial chemical reactions, but this would make potential experimental studies considerably more complex.

On the computational side, several numerical studies of anticonvection have been performed for the two-dimensional case [Simanovskii (1980), Simanovskii (2000), Simanovskii, Colinet, Nepomnyashchy, and Legros (2002), Simanovskii (2004)]. Three-dimensional simulations of anticonvection have not been reported so far with exception of the thesis of Merkt (2005), where some convective pattern are shown for the water-mercury system. In the present paper, we shall systematically study three-dimensional water-mercury anticonvection using direct numerical simulations with a pseudospectral two-layer code originally developed for the simulation of two-layer Marangoni convection. In particular, we provide first results on the strongly nonlinear regime far away from the threshold of anticonvection. Before discussing the simulation results in section 3, we summarize the governing equations and our numerical method in section 2. Conclusions are presented in section 4.

2   Mathematical model & numerical method

We consider a layered system of two immiscible liquids with thicknesses d_1 and d_2, where sub-

script 1 refers to the top layer and subscript 2 refers to the bottom layer. The interface between the liquids is located at $z = 0$, and the upper and lower bounding plates are at $z = d_1$ and at $z = -d_2$, respectively. We disregard the deformation of the interface. It has been shown recently that such deformations are incompatible with the Boussinesq approximation used in the present paper [Velarde, Nepomnyashchy, and Hennenberg (2001)].

Between the plates, the temperature difference ΔT is applied with $T = T_0 + \Delta T$ at the top plate and $T = T_0$ at the bottom plate. In the horizontal directions x and y we assume periodic boundary conditions with periodicity lengths L_x and L_y.

The material properties of the fluids are the dynamic viscosities μ_j, the kinematic viscosities ν_j, the densities ρ_j, the heat conductivities λ_j, the thermal diffusivities κ_j and the thermal expansion coefficients β_j, where $j \in \{1,2\}$.

We choose d_1 as the unit of length, ν_1/d_1 as the unit of velocity, d_1^2/ν_1 as the unit of time, $\rho_1 \nu_1^2/d_1^2$ as the unit of pressure, T_0 as reference temperature and ΔT as temperature unit. In the basic state of pure heat conduction, the temperature depends linearly on the vertical coordinate in each layer. Because of different thermal conductivities, the slope of the temperature profile changes at the interface. The conductive profile is

$$T_c(z) = \begin{cases} (\lambda + dz)/(\lambda + d) & 0 \le z \le 1, \\ \lambda(1 + dz)/(\lambda + d) & -1/d \le z \le 0, \end{cases}$$

(1)

where $f = f_1/f_2$ denotes the ratio of the values f_1 and f_2 of the corresponding parameter in the layers 1 and 2, respectively, e.g., $d = d_1/d_2$. We can now introduce the temperature perturbation

$$\theta = T - T_c(z)$$

(2)

as deviation from the distribution in the quiescent state. The velocity fields $\mathbf{v}_j = (u_j, v_j, w_j)$ and the temperature perturbations θ_j in each of the incompressible fluid layers are governed by the Navier-Stokes and energy equations. In Boussinesq approximation, and with our choice of units they

take the following dimensionless form

$$\partial_t \mathbf{v}_1 + (\mathbf{v}_1 \cdot \nabla) \mathbf{v}_1 = -\nabla p_1 + \nabla^2 \mathbf{v}_1 + G \mathbf{e}_z \theta_1, \quad (3)$$

$$\nabla \cdot \mathbf{v}_1 = 0, \quad (4)$$

$$P(\partial_t \theta_1 + (\mathbf{v}_1 \cdot \nabla) \theta_1) = \nabla^2 \theta_1 - \frac{Pd}{d+\lambda} w_1, \quad (5)$$

$$\nu(\partial_t \mathbf{v}_2 + (\mathbf{v}_2 \cdot \nabla) \mathbf{v}_2)$$
$$= -\mu \nabla p_2 + \nabla^2 \mathbf{v}_2 + \frac{G\nu}{\beta} \mathbf{e}_z \theta_2, \quad (6)$$

$$\nabla \cdot \mathbf{v}_2 = 0, \quad (7)$$

$$P\kappa(\partial_t \theta_2 + (\mathbf{v}_2 \cdot \nabla) \theta_2) = \nabla^2 \theta_2 - \frac{P\kappa d\lambda}{d+\lambda} w_2. \quad (8)$$

The separation of the linear conductive profile according to equation (2) gives rise to the linear terms proportional to w_j in equations (5) and (8). The Grashof number G and the Prandtl number P are defined by

$$G = \frac{\beta_1 g \Delta T d_1^3}{\nu_1^2}, \quad P = \frac{\nu_1}{\kappa_1}. \quad (9)$$

The boundary conditions complementing the evolution equations are

$$z = 1: \qquad \theta_1 = \mathbf{v}_1 = 0, \quad (10)$$

$$z = -1/d: \quad \theta_2 = \mathbf{v}_2 = 0 \quad (11)$$

at the top and bottom walls. At the liquid-liquid interface $z = 0$ the following conditions hold:

$$\theta_1 = \theta_2, \quad (12)$$

$$\partial_z \theta_2 = \lambda \partial_z \theta_1, \quad (13)$$

$$u_1 = u_2, \; v_1 = v_2, \; w_1 = w_2 = 0, \quad (14)$$

$$\mu \partial_z u_1 = \partial_z u_2, \quad (15)$$

$$\mu \partial_z v_1 = \partial_z v_2. \quad (16)$$

Conditions (12) and (13) imply the continuity of temperature and heat flux, conditions (14) describe the continuity of velocity and the non-deformability of the interface, conditions (15) and (16) reflect the balance of the interfacial shear components. Marangoni forces are neglected. The equations are solved using the parallel numerical code discussed in [Boeck, Nepomnyashchy, Simanovskii, Golovin, Braverman, and Thess (2002)]. It is based on a Fourier-Chebyshev expansion of the hydrodynamic fields in each of the liquid layers. The horizontal boundary conditions are periodic.

3 Numerical results

3.1 Convection near the instability threshold

For the water-mercury system we use the material properties listed in Table 1. These values apply for an ambient temperature of $10°\,$C. The density ratio ρ is then given by $\rho = \mu/\nu \approx 0.07367$. The Prandtl number of mercury is $P\kappa/\nu \approx 0.027$.

The ratio of thicknesses d is fixed to $d = 1$ in our present study. For this case, linear theory predicts the onset of steady convection for $G_c = 2010.5$ with a critical wavenumber $k_c = 0.97$.

Table 1: Ratios of material properties used in the simulations.

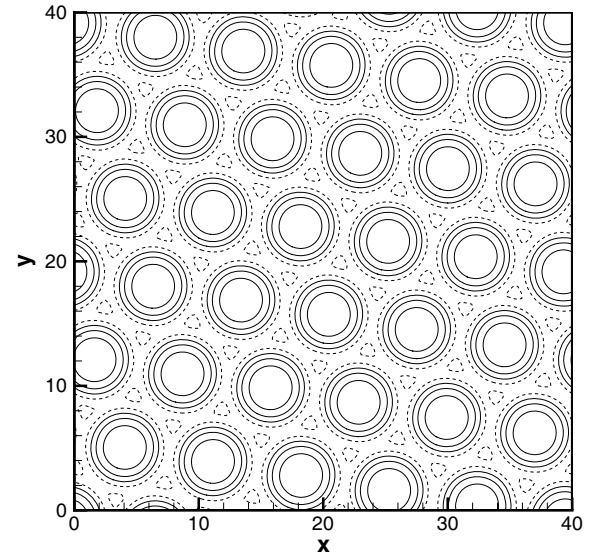| ν	μ	λ	κ	P	β
10.941	0.806	0.0685	0.0311	9.44	0.4906

Figure 1: Interface temperature distribution for $G = 2050$. Numerical resolution is $N_x = N_y = 128$ Fourier modes in x and y. The number of Chebyshev polynomials is 32 in each layer. Dashed lines indicate a negative value of the temperature perturbation θ.

The expected convective planform near the instability threshold G_c is hexagonal due to the lack of up-down symmetry in the problem. Starting from

random initial conditions of small amplitude in a large domain with $L_x = L_y = 40$ we find the steady hexagonal pattern shown in Fig. 1. The selection of the proper wavelength can be verified by counting the number of hexagons in the domain and comparing it with the theoretical estimate based on the area

$$A_c = \frac{8\pi^2}{\sqrt{3}k_c^2} \qquad (17)$$

per hexagon with wavenumber k_c. The expression (17) originates from the Christopherson solution for hexagonal flow patterns [Chandrasekhar (1961)]. In our case we have $L_xL_y/A_c \approx 33.0$. The number of hexagons in Fig. 1 is 34.

To explore the properties of perfect hexagons with wavenumber k_c we have performed simulations in the elementary rectangular domain compatible with a perfect hexagonal pattern. This domain has the dimensions $L_x = 4\pi/k_c$, $L_y = 4\pi/k_c\sqrt{3}$ and contains two hexagons, as can be seen in Fig. 2. The additional benefit is that the number of Fourier modes can be reduced to $N_x = 32$ and $N_y = 16$, which reduces the computational cost of the simulations.

The results of these simulations with the small domain are summarized in Fig. 3. It shows the Reynolds number Re_1 of layer 1 as function of G. The Reynolds numbers are defined separately for each layer as

$$Re_i = \frac{d_i}{\nu_i} \left| \frac{1}{L_xL_yd_i} \int_0^{L_x} \int_0^{L_y} \int_0^{d_i} \mathbf{v}_i^2(x,y,z)\mathrm{d}x\mathrm{d}y\mathrm{d}z \right|^{1/2},$$

$$(18)$$

i.e., with the spatial rms velocity. In case of time-dependent flow, time-averaging is also applied to obtain Re_i. To construct Fig. 3, we have first systematically decreased G from a value slightly larger than G_c into the subcritical range below G_c. Simulations were started from the converged state for the neighboring value of G. Convection persisted down to $G_s \approx 1730$, i.e., the relative size of the subcritical range is $1 - G_s/G_c \approx 0.14$. This is much larger than in one-layer Marangoni convection, where the subcritical range is about 1% or less [Thess and Orszag (1995), Boeck and Thess (1999)].
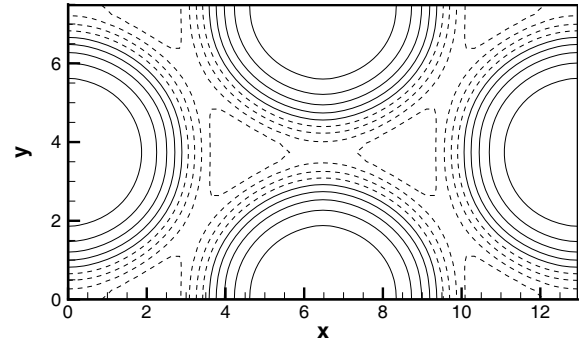

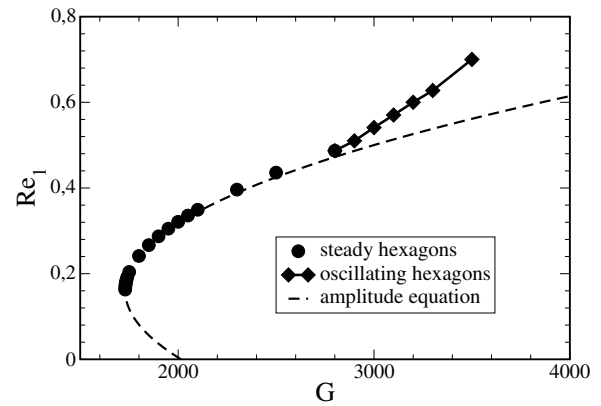Figure 2: Interface temperature distribution for $G = 2900$ in the small domain.

Figure 3: Reynolds number in the top layer as function of G for a small domain containing two perfect hexagons. The theoretical curve is a parabola in Re_1 in agreement with the leading terms in the amplitude equations for hexagons [Hoyle (2006)].
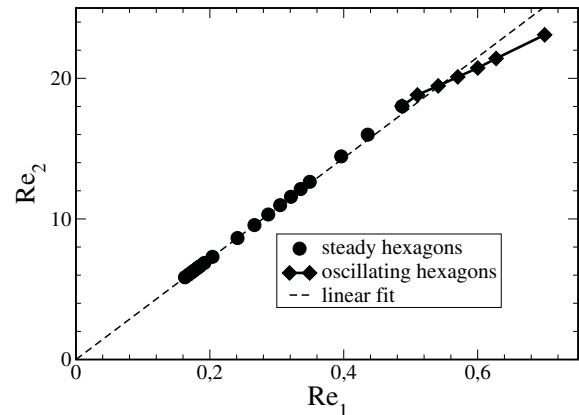

Figure 4: Reynolds numbers Re_1 in the top layer vs. Re_2 in the bottom layer for a small domain containing two perfect hexagons.

The hexagonal solutions have also been traced for increasing G. Oscillatory states appear around $G = 2900$. This solution branch departs visibly from the parabola representing the amplitude equation solution for steady hexagons. The particular properties of these oscillatory solutions are probably significantly affected by the small computational domain, and do therefore not necessarily reflect the behavior of the flow in larger cells. The oscillations are accompanied by a nonvanishing horizontal mean flow, which is oscillatory by itself. Mean flow dynamics may exhibit very slow transients, which can extend over 10^3 or more oscillation periods. We found such behavior, e.g., at $G = 3200$. The computational cost of such simulations can therfore be rather large, in spite of the moderate number of modes in the Fourier-Chebyshev expansion.

The appearance of the oscillatory solution branch is also apparent in Fig. 4. The oscillations produce a departure from the approximate proportionality between Re_1 and Re_2 for steady solutions. The Reynolds number Re_2 of the mercury also turns out to be significantly larger than Re_1, which is to be expected because of the very different material properties of the two liquids. We remark that the oscillatory solutions eventually become chaotic in the range $3500 < G < 3600$. The transition scenario has not been conclusively determined so far.

3.2 Strongly nonlinear convection

We shall now focus exclusively on the large computational domain with $L_x = L_y = 40$ used to obtain Fig. 1. As for the small domain, we can reduce G starting from $G = 2050$ in the simulations to trace the hexagonal solutions into the subcritical range. Again, the solution persists down to $G = 1730$. Likewise, the hexagonal pattern of Fig. 1 remains steady upon increasing G (in steps) to $G = 2600$. For $G = 2700$ the mean flow is excited, and the pattern starts to drift as a whole. We have found such behavior up to $G = 3000$. At $G = 3050$, the hexagonal pattern finally displays periodic oscillations with a period $T \approx 3.9$, which become chaotic at $G = 3100$. At $G = 3150$, the hexagonal pattern is replaced by a rhombic pattern with chaotic oscillations of local and global quantities. Fig. 5 shows a snapshot of this pattern. We remark that Merkt (2005) has apparently obtained stable square patterns, but for somewhat different liquid properties and at lower supercriticality, i.e., relative distance of G from the threshold G_c.

The change from a largely hexagonal to the rhombic pattern produces an increase in Reynolds numbers in each layer. This increase cannot be easily quantified for our large computational domain since the pattern does not settle into a steady state. We have unsuccessfully tried to obtain stable square patterns by reducing G and starting with the solution for $G = 3150$ as initial condition. An increase in G actually favors a return to a predominately hexagonal pattern at $G = 3200$. For $G = 3300$ and $G = 3500$ the pattern is more disorganized, and retains some domains where the cells are arranged in a square configuration.

Further increase of G destroys the remaining spatial order in the convective patterns, as can be seen in Fig. 6 for $G = 5000$. The typical size of the convective cells is significantly larger in Fig. 6 than in Fig. 5 or Fig. 1. This trend continues further upon increasing G to $G = 10000$ and $G = 20000$. Fig. 7 allows us to quantify this observation. It shows time-averaged spectra of the temperature distribution on the interface between the liquids. More precisely, $E_\theta(k)$ is calculated from the mean square of the absolute values of Fourier coefficients $\hat{\theta}_{\mathbf{k}}$ with a wavevector of given modulus, i.e.,

$$E_\theta(k) = \sum_{k - \Delta k < |\mathbf{k}| < k + \Delta k} |\hat{\theta}_{\mathbf{k}}|^2 \qquad (19)$$

in the discrete numerical representation. The wavenumber increment Δk is prescribed through the periodicity length $L_x = L_y = 40$ as $\Delta k = \pi/L_x$. The peak of E_θ is around $k \approx 1$ for $G = 3500$ and shifts to smaller values upon increasing G. For $G = 20000$, the decaying part of the spectrum can be approximated by a $k^{-3.5}$ power law for wavenumbers from the peak up to about $k \approx 3$, i.e., over about one decade in k. The spectra for lower G show a similar behavior over a shorter k-interval. The power law in Fig. 7 is drawn
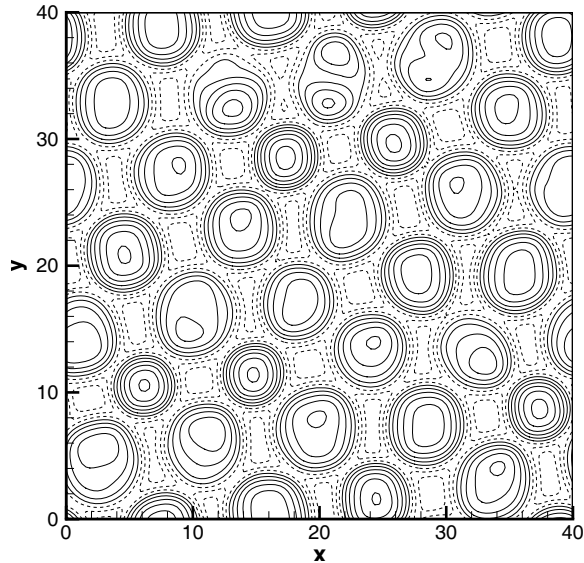
Figure 5: Interface temperature distribution for $G = 3150$. Numerical resolution is $N_x = N_y = 128$ Fourier modes in x and y. The number of Chebyshev polynomials is 32 in each layer.
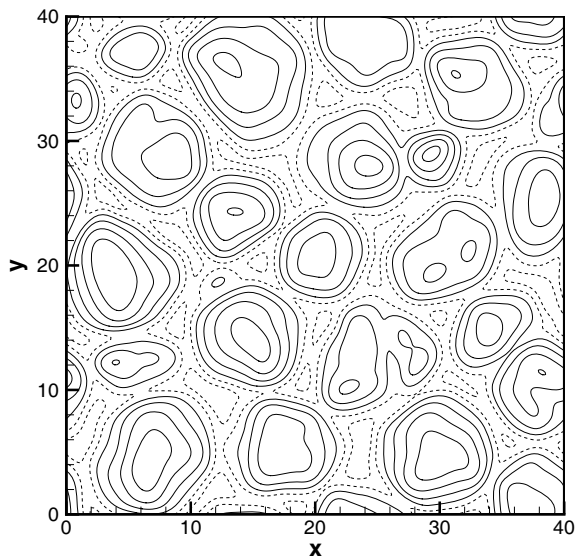

Figure 6: Interface temperature distribution for $G = 5000$. Numerical resolution is $N_x = N_y = 256$ Fourier modes in x and y. The number of Chebyshev polynomials is 32 in each layer.

for comparison, it does not represent a fit to the data. The growth of the spectra at large wavenumbers is due to aliasing errors of the pseudospectral method, and has no physical significance.

The growth of the rms velocities with G for the

time-dependent flows in the large domain is illustrated by plotting the Reynolds number Re_2 in the mercury layer as function of G in Fig. 8. The parabolic theoretical curve based on the cubic amplitude equations (as in Fig. 3) is shown for comparison. It is distorted by the logarithmic representation. The ratio between Re_1 and Re_2 continues to diminish at a relatively small rate upon increasing G in agreement with the trend of the oscillatory solution branch for the small aspect ratio case in Fig. 4.

3.3   *Vertical flow structure*

The vertical structure of the flow fields displays features in agreement with the instability mechanism described in the introduction. Fig. 9 shows a vertical cut through the two liquid layers in the plane $y = 0$ in Fig. 2, i.e., for the small domain with two hexagons at $G = 2900$.

As can be seen in Fig. 2, the plane $y = 0$ cuts through the center of a hexagon, which is located at the middle of the *x*-interval. The vertical velocity contours in Fig. 9 show that the mercury is rising in is region, and that isotherms are displaced towards the bottom, i.e., the temperature is elevated there. The velocity distribution in the water apparently corresponds to vertically stacked, counter-rotating vortices. The isotherms in the water layer also show a depression in the middle as expected from the descending flow near the interface. Since the mean temperature difference across the water layer is about ten times larger than for the mercury layer, the spacing of isotherms in the water is ten times that for mercury (in Fig. 9).

Vertical profiles of horizontal and vertical rms velocities are shown in Fig. 10 for the large domain. In the case $G = 20000$, spatio-temporal rms values are shown. We see that the stacked vertical structure in the water layer is preserved even at $G = 20000$, although the fluctuations render the averaged profiles smoother than in the case of stationary anticonvection. Another difference between the two cases is that at $G = 20000$ the horizontal rms velocity is larger than the vertical rms velocity for all z, whereas at $G = 1730$ it can be exceeded by the vertical rms velocity for certain
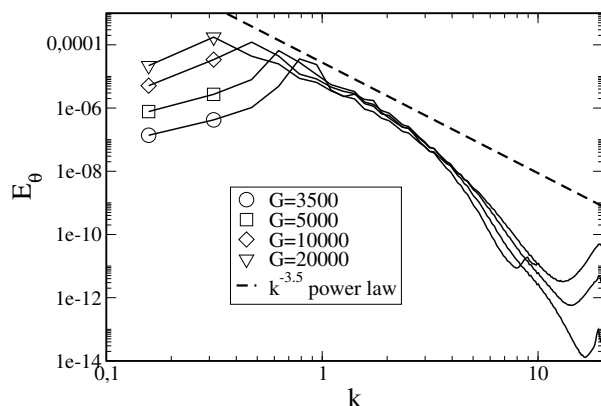
Figure 7: Temperature spectra on the interface.

Figure 8: Reynolds number Re_2 in the mercury for the large domain with $L_x = L_y = 40$.
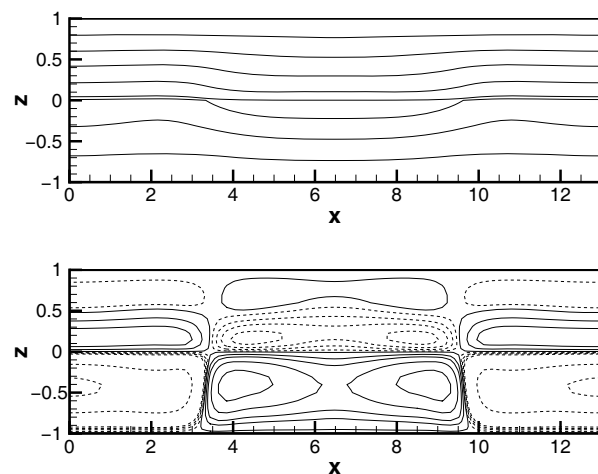

Figure 9: Isotherms (top) and isolines of vertical velocity (bottom) in a vertical plane. The spacing between isocontours is not equidistant. Dashed lines correspond to negative values.
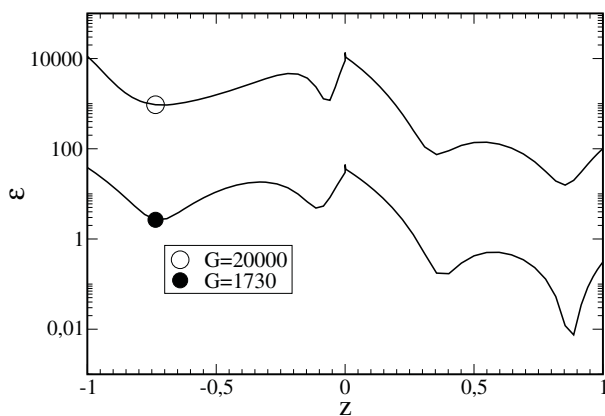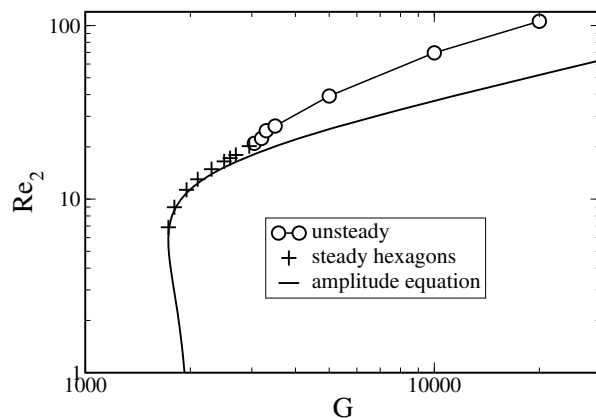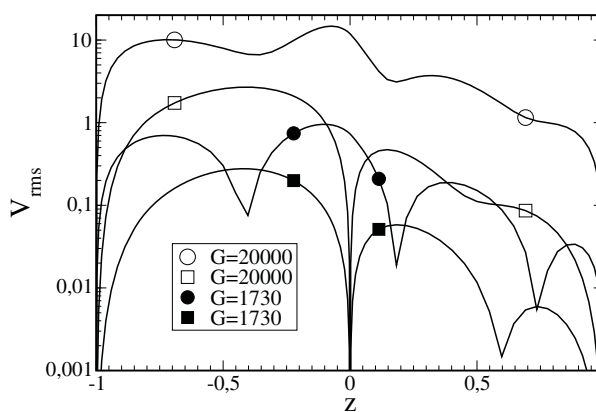

Figure 10: Vertical profiles of vertical and horizontal rms velocities for two different values of G. The square (round) symbols mark the profiles of vertical (horizontal) rms velocity.

Figure 11: Vertical profiles of the kinetic energy dissipation rate.
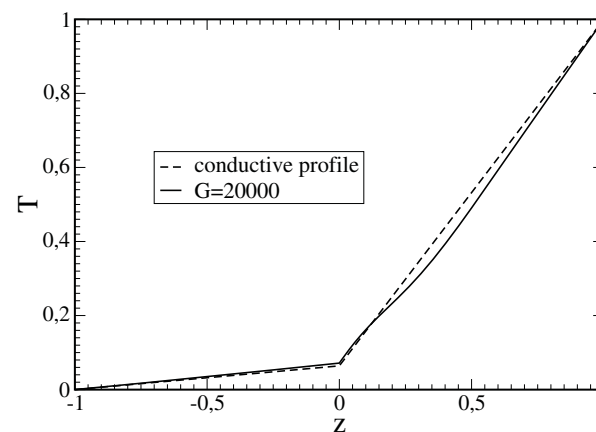

Figure 12: Mean temperature profile.

values of z. This observation is in line with the tendency of the convection cells to expand with the increase of G.

The mean kinetic energy dissipation rate ε is of interest for the kinetic energy budget of the flow. The dissipation rate of kinetic energy in layer i is defined (in dimensional units) as

$$\varepsilon_i = 2\rho_i \nu_i \sum_{kl} S_{kl} S_{kl}, \tag{20}$$

where k, l runs through the values x, y, z. The rate-of-strain tensor S_{kl} is defined by

$$2S_{kl} = \frac{\partial U_k}{\partial x_l} + \frac{\partial U_l}{\partial x_k}, \tag{21}$$

where U_l denotes the velocity component in co-ordindate direction l.

Vertical profiles of ε are shown in Fig. 11 for $G = 20000$ and $G = 1730$. They appear rather similar in spite of the large increase in G. In absolute values, about one third of the kinetic energy is dissipated in the water. In Fig. 11, ε is made non-dimensional with the units of the water (layer 1). Dissipation is strongest near the interface, but significant dissipation occurs also at the bottom of the mercury layer due to the strong shear caused by the no-slip condition. The appearance of a local minimum near the interface in the mercury layer is unexpected and has no obvious connection with features of the flow field discussed so far.

Kinetic energy is produced in the mercury layer due to the work by the buoyancy forces. In the water, this work is negative but rather small when compared with total energy production (about 20 times smaller).

Concerning the mean temperature profiles, it was already noted by Welander (1964) that the total heat flux does not change much by anticonvection, and that a plot of heat flux vs. temperature difference can probably not reliably detect anticonvection in an experiment. We cannot, therefore, expect a significant deviation from the conductive profile due to anticonvection. This conclusion is supported by the mean temperature profile for $G = 20000$ in Fig. 12, which differs only slightly from the conductive profile.

4   Conclusions

The paper presents nonlinear three-dimensional simulations of anticonvective flows in the water-mercury system. As explained above, the physical source of an anticonvective motion is the bulk buoyancy force (like in the case of the Rayleigh-Bénard convection), but nevertheless this type of convection is generated by the interface between the liquids (like in the case of the Marangoni-Bénard convection). Despite the unusual instability mechanism, the anticonvective patterns near the threshold are generic: they are hexagonal patterns which are developed in a subcritical way. With the growth of the Grashof number G, the hexagonal cells start to oscillate, first in periodic and then in a chaotic way, while keeping their spatial order. The further growth of G leads to a desorganization of patterns in space. The approximate $k^{-3.5}$ power-law decay of the interface temperature spectrum with the wavenumber k indicates that the distribution of horizontal temperature gradients organizes into rather flat patches connected by fairly abrupt "jumps", which produce a k^{-4} temperature spectrum as noted by Thess and Orszag (1995).

References

Boeck, T.; Nepomnyashchy, A.; Simanovskii, I.; Golovin, A.; Braverman, L.; Thess, A. (2002): Three-dimensional convection in a two-layer system with anomalous thermocapillary effect. *Phys. Fluids*, vol. 14, pp. 3899–3911.

Boeck, T.; Thess, A. (1999): Bénard-Marangoni convection at low Prandtl number. *J. Fluid Mech.*, vol. 399, pp. 251–275.

Chandrasekhar, S. (1961):   *Hydrodynamic and Hydromagnetic Stability*. Oxford University Press.

Hoyle, R. B. (2006):   *Pattern formation - An introduction to methods*. Cambridge University Press.

Merkt, D. (2005):   *Konventionsinstabilitäten und raumzeitliche Strukturbildung in Zweischicht-Systemen.* PhD thesis, Brandenburgische Technische Universität Cottbus.

Nepomnyashchy, A.; Simanovskii, I. (2001): Nonlinear investigation of anti-convection and Rayleigh-Benard convection in systems with heat release at the interface.   *Eur. J. Mech. B/Fluids*, vol. 20, pp. 75–86.

Nepomnyashchy, A.; Simanovskii, I. (2002): Combined action of anticonvective and thermocapillary mechanisms of instability. *Phys. Fluids*, vol. 14, pp. 3855–3867.

Nepomnyashchy, A.; Simanovskii, I.; Legros, J. C. (2006):   *Interfacial Convection in Multilayer Systems*. Springer, New York.

Nepomnyashchy, A. A.; Simanovskii, I. B.; Braverman, L. M. (2000):   Anticonvection in systems with heat release on the interface. *Phys. Fluids*, vol. 12, pp. 1129–1132.

Simanovskii, I.; Colinet, P.; Nepomnyashchy, A.; Legros, J. C. (2002):   Anticonvection with an inclined temperature gradient. *Phys. Rev. E*, vol. 66, pp. 056305.

Simanovskii, I. B. (1980):   *Convective stability of two-layer systems (in Russian)*. PhD thesis, Leningrad State University, Leningrad.

Simanovskii, I. B. (2000):   Combined action of anticonvective and thermocapillary mechanisms of instability in multilayer systems. *Eur. J. Mech. B/Fluids*, vol. 19, pp. 123–137.

Simanovskii, I. B. (2004):   Combined action of anticonvection and thermocapillarity in two- and three-layer systems. *Comptes Rendus Mecanique*, vol. 332, pp. 597–604.

Thess, A.; Orszag, S. A. (1995):   Surface-tension-driven Bénard convection at infinite Prandtl number. *J. Fluid Mech.*, vol. 283, pp. 201–230.

Velarde, M. G.; Nepomnyashchy, A. A.; Hennenberg, M. (2001): Onset of oscillatory interfacial instability and wave motion in Benard layers. *Adv. Appl. Mech.*, vol. 37, pp. 167–238.

Welander, P. (1964):   Convective instability in a two-layer fluid heated from above. *Tellus*, vol. XVI, pp. 349–358.